# Effects of soil fabric on the triggering of static liquefaction – Implications on mine tailings

Srinivas Vivek Bokkisa

Georgia Institute of Technology, Atlanta, Georgia, USA

Jorge Macedo

Georgia Institute of Technology, Atlanta, Georgia, USA

Alexandros L. Petalas

Durham University, Durham, UK

Chloé Arson

Georgia Institute of Technology, Atlanta, Georgia, USA

ABSTRACT: Static liquefaction has been associated to the failure of several tailing storage facilities (e.g., the Brumadinho failure in 2019) and has been a persistent topic of discussion in the mining and tailings communities. Experimental studies have suggested that the onset of static liquefaction is dependent on the initial state (void ratio and confinement), and fabric anisotropy. In this context, traditional constitutive models developed under the critical state theory (CST) have been used to investigate the onset of static liquefaction for several complex loading paths. However, these models do not capture the effect of soil fabric anisotropy (inherent and induced) that are relevant in field conditions. In this study, the Anisotropic Critical State Theory (ACST) framework is used to assess the onset of static liquefaction in particulate materials, incorporating the effects of inherent and induced fabric. Our assessments derive an analytical criterion to assess static liquefaction that can be applied for screening assessments. The derived analytical criterion is a function of material properties, state, and a fabric anisotropy, which couple the effects of fabric and loading direction. The use of the derived criteria in particulate materials is illustrated and the implications on assessing the static liquefaction of mine tailings under generalized loading is also discussed.

# 1 INTRODUCTION

The static liquefaction of mine tailings has caused numerous recent tailings storage facility (TSF) failures, such as the 2015 Fundao failure in Brazil, the 2018 Cadia failure in Australia, and the 2019 Brumadinho failure in Brazil. These failures have caused unprecedented devastating consequences for the environment, infrastructure damage, and loss of human life; they have been in the spotlight of the mining, engineering, and environmental communities. For example, the 2015 Fundao TSF failure is considered as the biggest unprecedented environmental disaster in Brazil.

Static/flow liquefaction in granular material is associated with a state of instability followed by sudden increases in strain and pore water pressure. It can occur in any saturated or near-saturated contractive materials, such as very loose sands, silts, as well as mine tailings. Previous research has suggested that the instability onset triggers at a characteristic stress ratio. This concept is illustrated in Figure 1a using undrained triaxial tests from Lade (1999). In particular, Lade (1999) highlighted that the stress state at the point of instability for samples with the same initial density but under different confining stresses are aligned on a unique line called the instability line. This so-called instability line represents the stress conditions in which flow liquefaction triggers, leading to the potential instability region shown in Figure 1a.

Experimental studies have highlighted the role of the rotation of principal stress axes ( $\alpha_{\sigma}$ ) and the intermediate stress ratio (b) on the onset of flow liquefaction. For example, Yoshimine et al. (1998) and Georgiannou & Tsomokos (2008) used the hollow cylinder apparatus to evaluate the influence of principal stress direction and intermediate principal stress on the onset of flow liquefaction. A typical hollow cylinder element and the corresponding stress state are shown in Figure 1b. The experimental studies consistently showed that sand specimens that were loaded under a

large intermediate principal stress or under a large rotation of the principal stress axis had a lower instability stress ratio. Other studies have also highlighted the role of initial fabric on instability triggering. For instance, Miura & Toki (1982), Yang et al. (2008), and Sze & Yang (2014) showed that specimens prepared following different reconstitution methods while maintaining similar loading conditions exhibited significantly different behaviors, highlighting the initial fabric effects.

The instability onset associated with flow liquefaction has also been studied numerically and analytically, with more efforts focusing on triaxial conditions. For example, Najma & Latifi (2017) used undrained stress paths and the instability definition at their peak to derive an instability criterion in terms of hardening modulus. A closed formulation was obtained for the model of Dafalias and Manzari (Dafalias & Manzari, 2004) and other constitutive models, focusing on triaxial conditions. This work was later expanded (Najma & Latifi, 2017, 2018), considering the multiaxial version of the model by Dafalias & Manzari (2004). These previous studies have emphasized that the predictive performance of the different instability criteria depends on that of the constitutive model at play. Thus, including fabric anisotropy effects has not been feasible in these previous studies due to the limitations of the constitutive models employed.

In this study, we derive an analytical instability criterion for granular materials under undrained loading by using the relatively new anisotropic critical state theory (ACST). The criterion is established using the SANISAND-F model, and it is amenable to incorporating the effects of inherent and induced fabric. We use the established criterion to numerically assess different alternatives to investigate the effects of fabric anisotropy in triggering instability. We explore the effects of the rotation of principal stress direction, intermediate stress ratio, and the initial fabric intensity on the slope of the instability line estimated from the criterion.

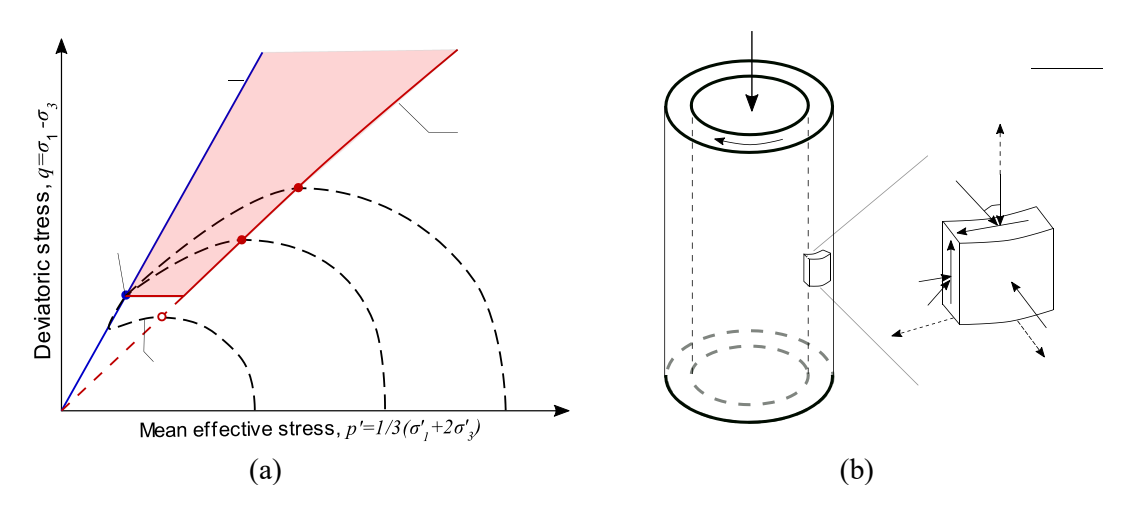


Figure 1 (a) Illustration of Instability line in a p'-q space, considering undrained triaxial compression tests. Modified from Lade (1999) (b) Element in a hollow cylinder specimen showing stress components and highlighting principal stress rotation  $\alpha_{\sigma}$  and intermediate stress-ratio b.

#### 2 THE SANISAND-F MODEL

The SANISAND-F model was recently proposed by Petalas et al. (2020). It is an extension of the critical two-surface plasticity model presented in Dafalias & Manzari (2004). The model is formulated within the ACST (Li & Dafalias, 2012), which accounts for the effect of fabric anisotropy on the mechanical behavior of granular soils. For a detailed presentation of the model and the ACST, the reader is referred to Li & Dafalias (2012) and Petalas et al. (2020).

In addition to the features of the DM04 (Dafalias & Manzari, 2004) model, the SANISAND-F model utilizes a deviatoric fabric tensor  $\mathbf{F}$  as an evolving state variable. A scalar-valued Fabric Anisotropy Variable,  $A = \mathbf{F} : \mathbf{n}'$ , is then introduced as a measure of relative orientation between

loading (n') and fabric directions (F). The original critical state conditions are enhanced as proposed in Li & Dafalias (2012) via  $A = A_c = 1$ , which denotes that at critical state the fabric and loading direction coincide. The isotropic state parameter  $\psi$  (Been & Jefferies, 1985) is enhanced with the effect of fabric via the dilatancy state parameter  $\zeta$ . The new state parameter determines the estimated dilatancy, which depends on fabric anisotropy, and the model's response becomes more contractive as the difference in fabric and loading orientation increases. In this study, we used the material parameters suggested by Petalas et al. (2020) (see Table 1), who calibrated the model against the experimental results from Yoshimine et al. (1998). Figure 2 shows the performance of SANISAND-F model in comparison to DM04 model when compared to experimental results in triaxial compression and extension tests. It can be observed that the DM04 model cannot predict the onset of static liquefaction in triaxial extension experiments. In contrast, SANISAND-F model match both triaxial compression and extension test results.

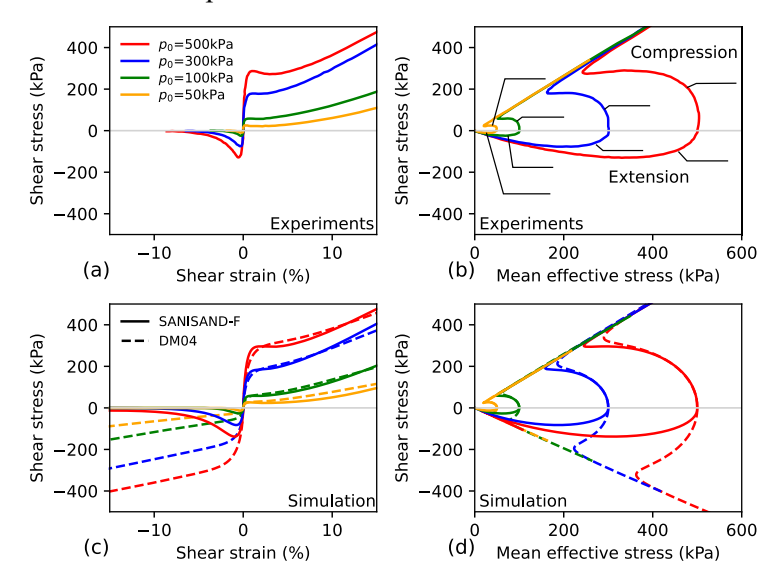


Figure 2 Performance of SANISAND-F in comparison to DM04 model

**Table 1 SANISAND-F parameters** 

Description	Symbol	Values
Elasticity	$G_0$	125
	v	0.05
Critical state	$e_{ref}$	0.934
	ξ΄ λ	0.7
	λ	0.019
	$M_{c}$	1.25
	c	0.75
Plastic modulus	$h_1$	7.5
	$c_h$	0.85
	$n^b$	1.4
Yield surface	m	0.01
Dilatancy	$A_0$	0.704
	$n^d$	3.5
Fabric	$e_A$	0.0818
	$F_{in}$	0.5
	$c_0$	5.2
	$h_2$	1.3
	$oldsymbol{n}_F$	[2/√6 0 0 ]
		$0 -1/\sqrt{6} 0$
		$\begin{bmatrix} 0 & 0 & -1/\sqrt{6} \end{bmatrix}$

## 3 FLOW LIQUEFACTION INSTABILITY CRITERION

Analytical flow instability criteria can be derived using the fabric-dependent multi-axial SANI-SAND-F constitutive model for undrained loading following the procedure presented in Najma & Latifi (2017). Two main conditions can be used to derive the instability criterion from the SANI-SAND-F equations; the first is the undrained loading condition where the rate of volumetric strain is zero, i.e.,  $d\epsilon_v = 0$  and second is the condition of the slope of undrained stress path at instability point on the stress space is zero, i.e., dq/dp = 0. Using these two conditions, two instability criteria can be derived, i.e.,  $H_1 = K_p - K_{p,f} = 0$  and  $H_2 = \beta - \beta_f = 0$ . Where  $K_p$  is the current plastic modulus and  $K_{p,f}$  is the estimated plastic modulus at the instability point. Similarly,  $\beta$  is the current stress-ratio and  $\beta_f$  is the estimated stress-ratio at the instability point. More details on the step-by-step procedure of the derivation of instability criterion are presented in Bokkisa et al. (2022).

Figure 3a and 3b show the evolution of the instability criteria  $H_1$  and  $H_2$  while Figure 3c and 3d show the stress-strain response of numerical simulations performed at an initial void ratio of 0.89, and confining stress of  $p_0 = 500 \ kPa$  for a hollow cylinder loading path with constant principal stress direction,  $\alpha_{\sigma} = 45^{\circ}$ , and intermediate stress ratio, b = 0.5 (refer Fig. 1b for  $\alpha_{\sigma}$  and b). It can be observed that the first criterion yields two instances where  $H_1 = 0$  (see Figure 3a): the first point marks the onset of flow liquefaction, while the second represents a change from contractive to dilative behavior, also known as the transformation point (Andrade et al., 2013, Ishihara, 1993). Note that the two-criterion used for the instability assessment, i.e.,  $d\epsilon_v = 0$  and dq/dp = 0 also gets satisfied at the transformation point, hence the  $H_1$  criterion results in two points. By contrast, the  $H_2 = 0$  criterion (see Fig. 3b) predicts only the onset of flow liquefaction point. Note that both  $H_1$  and  $H_2$  criteria are consistent in identifying the onset of flow liquefaction, and from here on,

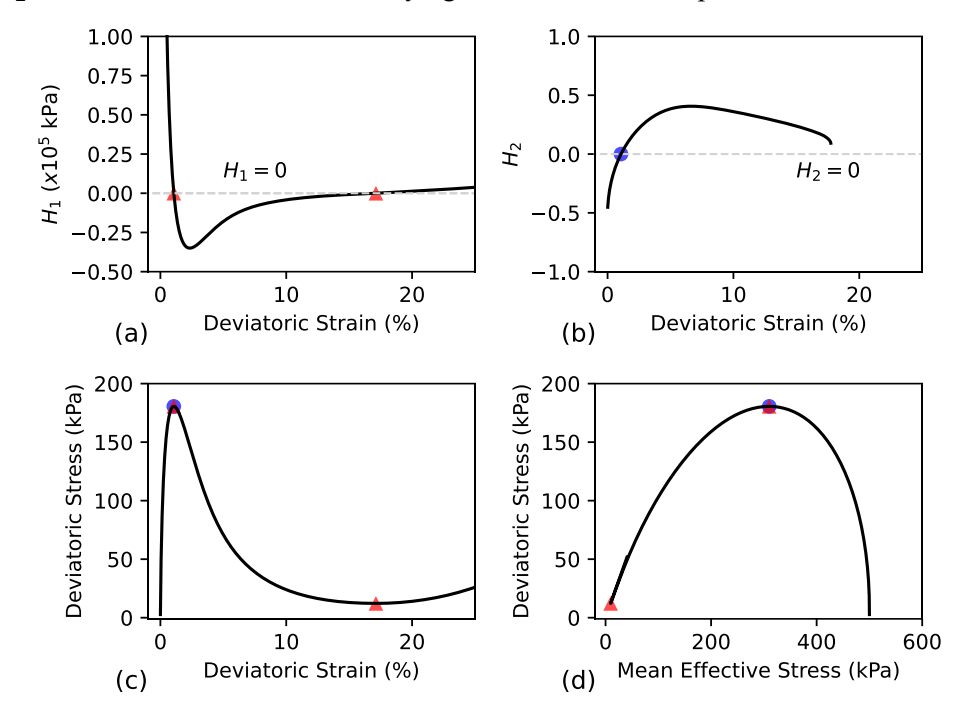


Figure 3 SANISAND-F simulation of a hollow cylinder test (a & b) the  $H_1$  and  $H_2$  criterion (c&d) stress-strain and stress path response

unless specified, we use only the  $H_2$  criterion to predict flow liquefaction instability point.

Next, to illustrate the concept of an instability surface, we conduct simulations at constant  $\alpha_{\sigma} = [0^o, 45^o]$  and varying the Lode angle,  $\theta$ , with values from  $0^o$  to  $360^o$ . Note that if the principal stresses are in the order  $\sigma_{11} > \sigma_{22} > \sigma_{33}$ , the intermediate stress ratio is given by  $b = (\sigma_{22} - \sigma_{33})/(\sigma_{11} - \sigma_{33})$ , which is also related to the Lode angle,  $\theta = \frac{\pi}{6} + \tan^{-1}(\frac{2b-1}{\sqrt{3}})$ . The instability points predicted from these simulations can be plotted in a  $\pi$ -plane of the deviatoric stress-ratio space to visualize an instability surface, as shown in Figure 4. Note that the Lode angle  $\theta = 0^o$ 

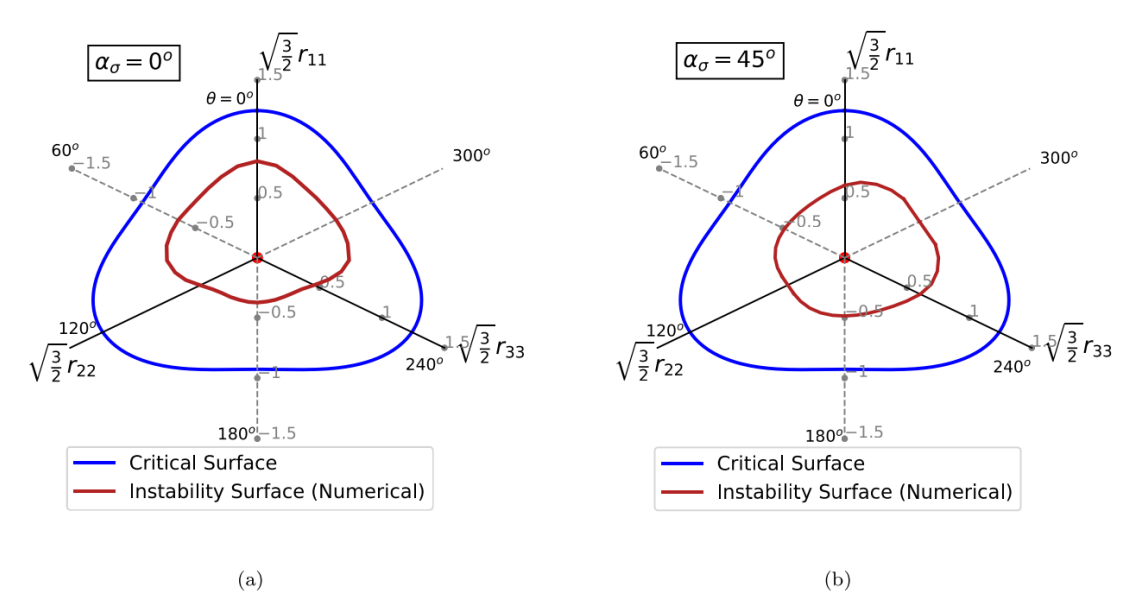


Figure 4 Instability surface obtained from the numerical simulations of a hollow cylinder test with constant Lode angle ( $\theta$ ) and constant stress principal axis rotation ( $\alpha_{\sigma}$ ) using Toyoura sand properties with e=0.89 and  $p'_{in}=500$  kPa (a) for  $\alpha_{\sigma}=0^o$  (b) for  $\alpha_{\sigma}=45^o$ 

corresponds to b=0 while  $\theta=60^o$  corresponds to b=1. For  $\theta>60^o$  only the Lode angle will be used to refer to the loading path. The instability surface separates the stable stress states from the unstable stress states in terms of flow liquefaction. Interestingly, it can be observed that the instability surface is not symmetrical with respect to all the major axes in the stress space (i.e., the  $\theta=0^o$ - $\theta=180^o$ ,  $\theta=60^o$ - $\theta=240^o$ , and  $\theta=120^o$ - $\theta=300^o$  axes), as typically observed in constitutive models under the classical critical state framework (e.g., DM04). This is attributed to the effect of fabric anisotropy that is incorporated by the ACST framework. Note that when  $\alpha_\sigma=0^o$  the instability surface is symmetrical with respect to the major axes,  $\theta=0^o$ - $\theta=180^o$  in stress space (refer Figure 4). This is due to the fact that when  $\alpha_\sigma=0^o$  the principal axes of loading and fabric tensor align with each other thus allowing symmetry in the horizontal directions.

# 4 STRESS PRINCIPAL AXIS ROTATION, LODE ANGLE, AND FABRIC EFFECTS ON THE ONSET OF STATIC LIQUEFACTION

A series of numerical simulations with varying stress principal axis rotations  $(\alpha_{\sigma})$ , Lode angle  $(\theta)$ , and initial fabric intensity  $(F_{in})$  are performed in this section to investigate their effect on the triggering of flow instability. Note here that stress principal axis rotation represents the constant and fixed rotation of  $\alpha_{\sigma}$  during undrained shearing. Moreover, undrained hollow cylinder experiments performed by Yoshimine et al. (1998) are simulated for validation of the modeling procedure. All the simulations are done with SANISAND-F using the set of material parameters presented in Table 1.

# 4.1 Effect of principal stress axis rotation $\alpha_{\sigma}$

Figure 5 presents the simulation results of tests with initial void ratios in the range of 0.821-0.828, initial confinement  $p_0' = 100$  kPa,  $\theta = 30^{\circ}$  (b = 0.5), and different  $\alpha_{\sigma}$  values i.e.,  $[15^{\circ}, 30^{\circ}, 45^{\circ}, 60^{\circ}, 75^{\circ}]$ . The experimental results from Yoshimine et al. (1998) are also presented for comparison. In the experiments, the instability point (marked with an open circle) corresponds to the local peak in the p' - q space. The  $H_2$  instability criterion is also tracked for the numerical simulations, and the open circles on the numerical-based curves correspond to the stress ratios satisfying it.

The increasing contractive behavior with the increase of  $\alpha_{\sigma}$  is well captured by the SANI-SAND-F model, which also reproduces with acceptable accuracy the stress-strain response as also discussed in Petalas et al. (2020). In all cases, after the flow instability point, a phase transformation from a contractive to a dilative tendency is observed. This response is also well captured by the model.

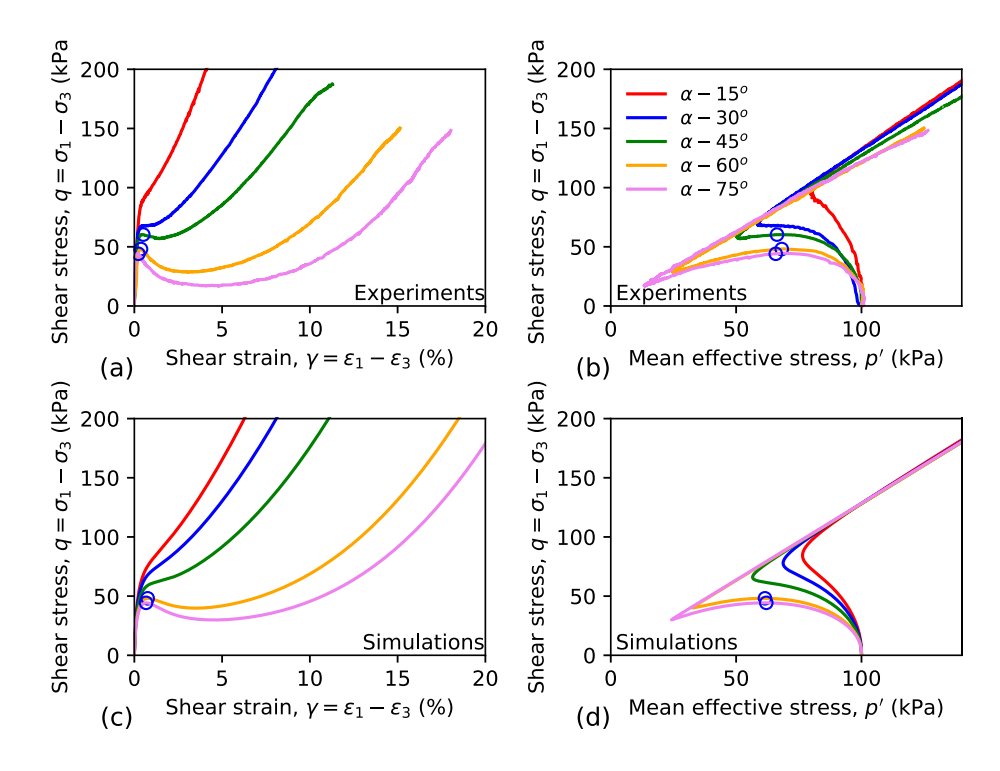


Figure 5 Experimental data (a,b) and SANISAND-F simulations (c,d) for undrained shearing with constant  $\theta$ =30°0 (b=0.5) and constant  $\alpha_{\sigma}$ =15°0-75°0 on Toyoura sand with e=0.821-0.828. Data from Yoshimine et al. (1998)

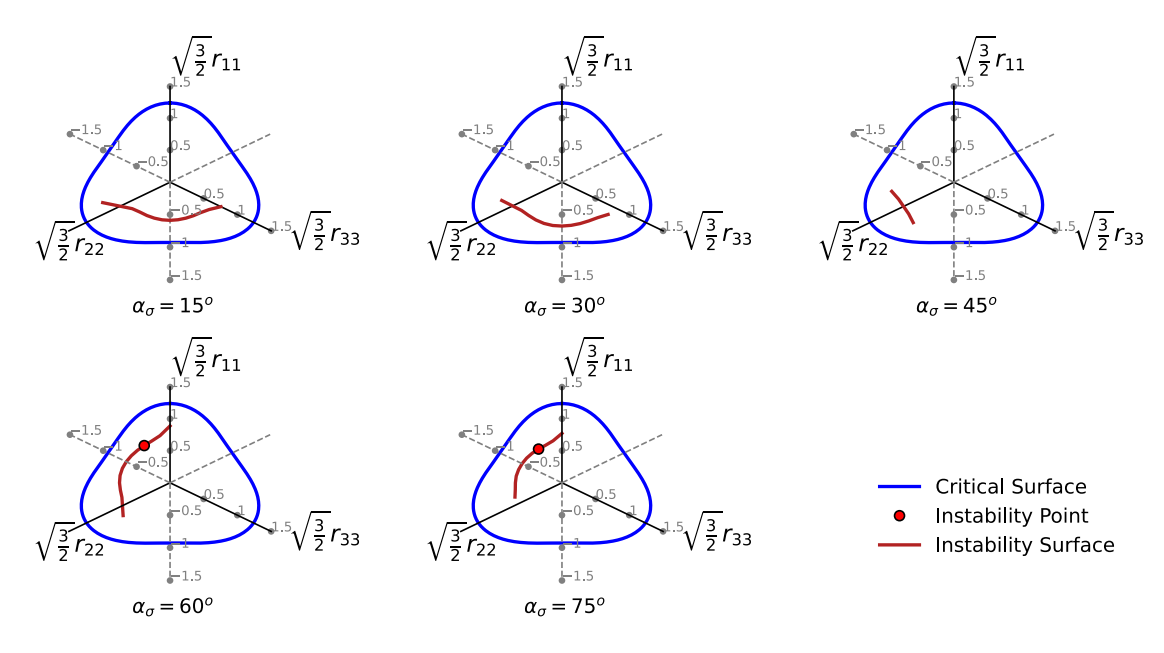


Figure 6 Numerical estimation of instability surfaces for tests with constant  $\alpha_{\sigma} = [15^{o} - 75^{o}]$  on Toyoura sand with e = 0.821 - 0.828. Instability points corresponding to b = 0.5 ( $\theta = 30^{o}$ ) are plotted on instability surfaces when defined (for  $\alpha_{\sigma} = 60^{o}$  and  $\alpha_{\sigma} = 75^{o}$ )

Figure 6 shows the instability surfaces on the deviatoric plane estimated for loading paths with different  $\alpha_{\sigma}$ , using the procedure discussed in Section 3. Note that the instability surface is discontinuous due to the fact that flow instability does not occur for every combination of angles  $\theta$ and  $\alpha_{\sigma}$ . For example, the surface is not defined for  $\theta = 30^{\circ}$  when  $\alpha_{\sigma} = 15^{\circ}$ ,  $30^{\circ}$ , and  $45^{\circ}$  (i.e., there is no instability onset), but it is defined for  $\alpha_{\sigma}=60^{\circ}$  and 75°, which is consistent with the results in Figure 5. Of note, instability may be still triggered for other  $\theta$  values (i.e., other loading paths) where the instability surface is defined when  $\alpha_{\sigma}=15^{\circ}$ , 30°, and 45° as illustrated in Figure 6. Interestingly, for a loading path in the downward  $r_{11}$  direction (i.e.,  $\theta = 180^{\circ}$ ), we can see that there is an instability onset for  $\alpha_{\sigma} = 15^{o}$ , but not for  $\alpha_{\sigma} = 75^{o}$ , which is apparently in contrast with the observations in Figure 5. However, this observation is associated with the coupled effects between the loading direction and fabric orientation. The quantity N = n':  $n_F$  measures the relative orientation between the fabric and loading directions. If the fabric and loading have the same direction (i.e., N = 1), the computed behavior shows a hardening response. As the difference between the fabric and loading directions increases a softening response is enhanced. These observations are consistent with the results in Figure 5. where as  $\alpha_{\sigma}$  decreases N increases (i.e., it gets close to 1), causing an enhanced hardening response. For the  $\theta = 180^{\circ}$  loading path, when  $\alpha_{\sigma}=15^{o}$  the initial value of N is -0.89, causing a softening response that triggers an instability condition. Whereas when  $\alpha_{\sigma}$ =75° the initial value of N is 0.41, causing a hardening behavior with no instability triggering.

#### 4.2 Effect of lode angle $\theta$ (or intermediate stress ratio b)

Figure 7 shows the SANISAND-F simulations of undrained tests on Toyoura sand with void ratio e = 0.855, initial confinement  $p'_0 = 100$  kPa,  $\alpha_{\sigma}$  equal to  $45^{\circ}$ , and different  $\theta$  values, i.e.,  $[0^{\circ}, 13.9^{\circ}, 30^{\circ}, 46.1^{\circ}, 60^{\circ}]$  (corresponding to b = [0,0.25,0.5,0.75,1]) using the same set of parameters as in previous simulations (i.e., Table 1). The experimental results from Yoshimine et al. (1998) are also presented for reference. Note the void ratio in experiments varies from e = 100

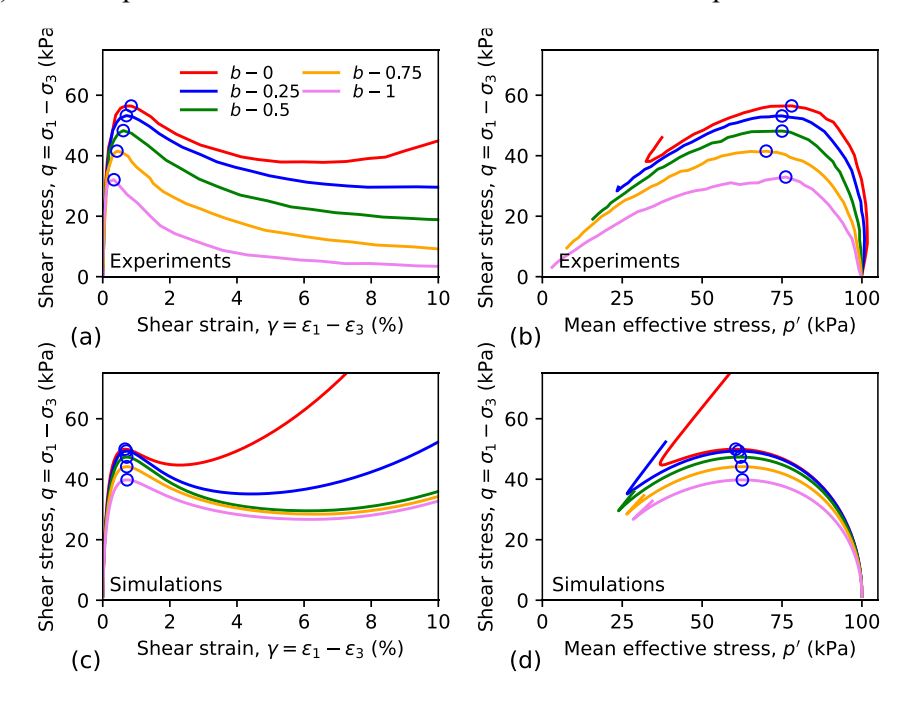


Figure 7 Experimental data (a,b) and SANISAND-F simulations (c,d) for undrained shearing with constant  $\alpha_{\sigma} = 45^{o}$  and constant b = 0 to 1 on Toyoura sand with e = 0.855. Data from Yoshimine et al. (1998)

0.849-0.861. A representative mid-value for the void ratio of e=0.855 is selected for simulations. The numerical results are qualitatively consistent with the experimental results, i.e., as the b value increases, a more contractive response with lower peak values is observed. Notice also that there are more differences in the dilatancy response (i.e., experimental versus numerical) at large strains for large b values, which may be attributed to the dilatancy scaling in SANISAND-F. However, in assessing instability conditions, the post-peak response is, comparatively, not as important as assessing the triggering (Sadrekarimi, 2014). The instability points estimated by the criterion  $H_2$  are also presented in Figure 7. The estimated instability surface for  $\alpha_{\sigma} - 45^{\circ}$  is presented in Figure 8, which also shows the instability points for different b values. In Figure 7, instability triggers for all the considered b values, which is consistent with Figure 8. In addition, the instability stress ratios (i.e., the distance from the instability surface to the origin) decrease as b increases, which is in agreement with the previous discussions. For higher Lode angles, i.e.,  $\theta$  from  $250^{\circ}$  to  $350^{\circ}$ , the simulations show hardening responses, and thus the instability surface is not defined.

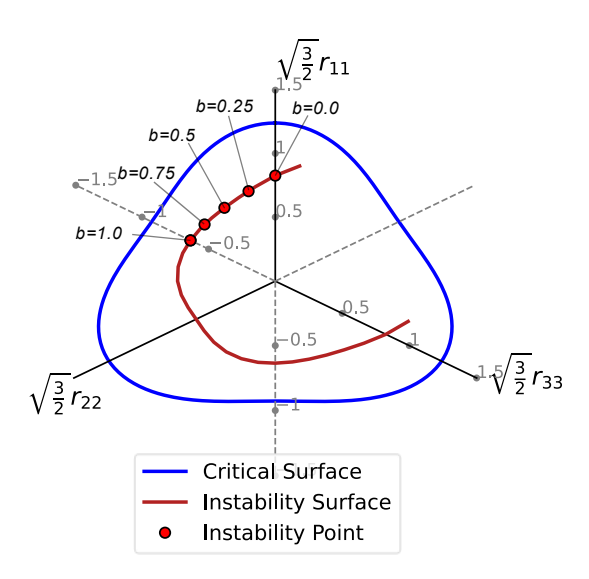


Figure 8 Numerical estimation of instability surfaces for tests with constant  $\alpha_{\sigma}=45^{o}$  on Toyoura sand with e=0.855. Instability points corresponding to b=0-1 are plotted on instability surfaces

## 4.3 Initial soil fabric effects

To assess the effect of the initial fabric on the instability surface. A sensitivity analysis is performed using different fabric intensities for the initial cross-anisotropic fabric direction. Figure 9 (a) and (b) show the undrained constitutive response obtained for a constant loading path with  $\alpha_{\sigma} = 0^{o}$  and  $\theta = 0^{o}$  (triaxial compression loading), a void ratio e = 0.89, an initial confinement pressure  $p'_{0} = 500$  kPa, and a variable initial fabric intensity  $F_{in} = [0.01,0.5,1.0]$ , which includes the typical range of  $F_{in} = 0 - 0.6$  for Toyoura sand in different sample preparation methods (Gao & Zhao, 2015). Note that  $F_{in} = 0.01$  represents a nearly isotropic fabric and  $F_{in} = 1.0$  represents a highly anisotropic fabric. Such extreme fabric intensities are chosen along with the value  $F_{in} = 0.5$  (recommended in Petalas et al. (2020)) to highlight the influence of initial fabric on a wide range. It is observed that the constitutive behavior becomes more dilative as the fabric intensities increase from 0.01 to 1.0 (see Figure 9a,b). In fact, for a fabric intensity of  $F_{in} = 1.0$ , there is no instability point detected. This is because, in the ACST framework the fabric anisotropy variable, A = FN, controls the contractive (lower value of A) or dilative (higher value of A) behavior of the constitutive response in undrained loading. Where F is the fabric intensity and N is the relative orientation between fabric and loading directions. For the three cases in Figure 9(a,b), the value of  $N = n_F$ : n' is equal to 1, this is because the cross-anisotropic fabric (triaxial compression like fabric direction) and the triaxial compression loading have the same orientation. Thus, the value

of A is equal to F and for higher initial fabric intensity the constitutive response is more dilative and the instability stress-ratio is higher. Figure 9(c) and (d) show the results of numerical simulations conducted with constant  $\alpha_{\sigma} = 0^{o}$  and  $\theta = 180^{o}$ . It is now observed that the fabric intensity has an inverse effect on the constitutive response and the instability stress-ratio compared to the triaxial compression loading path. This is because, for the new loading path, the value N = -1, implying A = -F, and thus causing the inverse effect. This highlights that the overall observed response (e.g., the instability triggering) is intimately related to coupled effects between the initial

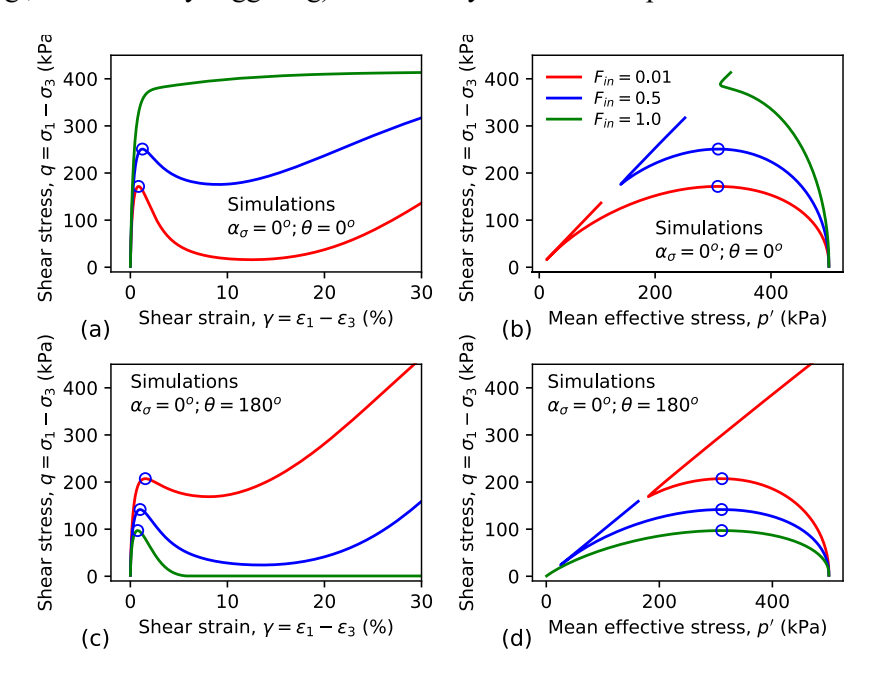


Figure 9 SANISAND-F simulations of undrained shearing with initial state of e=0.85, p\_in^'=500 kPa and different fabric intensities F\_in=[0.01,0.5,1.0] subjected to constant  $\alpha_{\sigma}=0^{\circ}$  and  $\theta=0^{\circ}$  in (a) and constant  $\alpha_{\sigma}=45^{\circ}$  and  $\theta=0^{\circ}$  in (b).

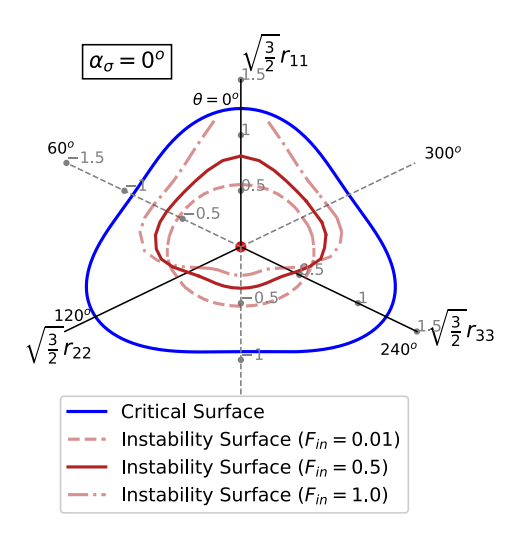


Figure 10 Effect of initial fabric intensity on the instability surface obtained for various loading paths,  $\theta$  varying from  $0^o$  to  $360^o$  with constant  $\alpha_{\sigma} = 0^o$ 

fabric and the imposed loading paths, which is at the core of the ACST framework. This is further

illustrated in Figure 10, which shows the effect of fabric intensity on the instability surface represented in the  $\pi$ -plane for loading paths with constant  $\alpha_{\sigma}=0^{o}$ . The effect of initial fabric intensity is clearly evident from the shapes of the instability surfaces. For  $\alpha_{\sigma}=0^{o}$ , the highest influence of fabric intensity on the instability point is observed for loading paths with  $\theta$  values close to zero. The initial fabric effects at other loading paths, such as  $\theta=60^{o}$ ,  $\theta=180^{o}$ ,  $\theta=300^{o}$  are also substantial.

#### 5 IMPLICATION TO MINE TAILING DEPOSITS

In previous sections, the effects of inherent and induced fabric are assessed considering mechanical properties corresponding to Toyoura sand, but it is worthwhile highlighting that the constitutive models developed under the ACST framework are expected to be suitable for any particulate materials, including mine tailings, once the corresponding mechanical properties are accounted for (Macedo and Vergaray, 2022). Thus, the qualitative observations discussed in previous sections are expected to hold for mine tailings. In this context, having well-calibrated SANISAND-F material parameters for different mine tailings gradations would allow quantifying typical responses for mine tailings where fabric anisotropy is included.

In the design or condition assessment of TSFs, a geotechnical engineer is usually in charge of evaluating the TSF's response to static liquefaction, which is an engineering aspect of major interest. Fabric effects, which are expected to play an important role, are often ignored as it is difficult to account for them in engineering practice; however, the ACST framework with well-calibrated models opens an avenue for incorporating fabric effects on engineering assessments. In highlighting the importance of fabric effects, Figure 11 shows the state of stresses schematically on the upstream deposited tailings on the Fundao dam that failed on 2015. It can be observed that along the slope, different stress states like triaxial compression, rotated principal stresses, simple shear, and triaxial extension are exhibited. It is expected that the inherent tailings fabric, in combination with the different loading paths and different initial consolidation states, played an important role in the static liquefaction instability triggering under the considerations discussed in previous sections of this paper. The proposed analytical criterion in this study is a step forward for incorporating inherent and induced fabric effects once mechanical properties are quantified.

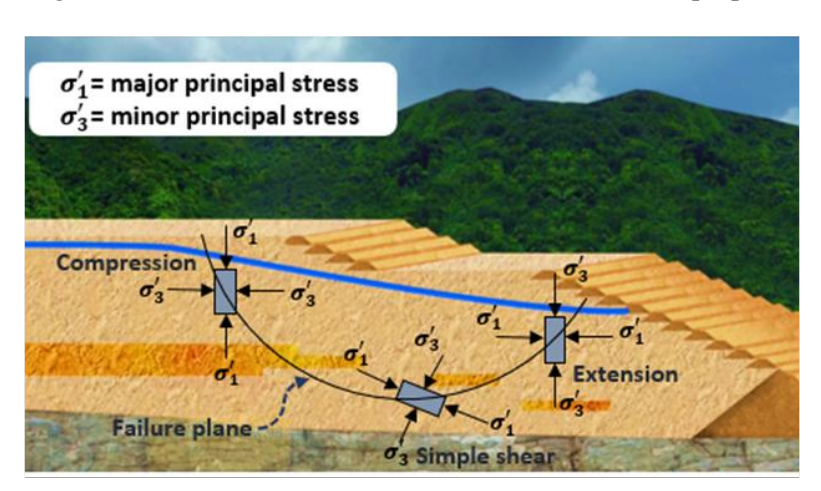


Figure 11 Schematic representation of the stress states under the Fundao tailings dam that failed in 2015

#### 6 CONCLUSIONS

In this study, the static liquefaction triggering in particulate materials under undrained loading conditions is investigated, considering the role of state, multiaxial loading, and fabric anisotropy. It was shown that the ACST framework provides benefits to account for generalized loading and

fabric effects, which are also expected to be of major importance on mine tailings. In this context, we derived criteria that predict instability conditions for generalized undrained loading, including anisotropy and fabric effects. An interesting finding is that the instability surface constructed using the derived criteria is not hexagonally symmetrical with respect to the origin in the stress space, which is expected to also hold true for mine tailings. This is due to the fact that within the ACST framework, the relative effects of soil fabric and the loading direction are taken into account in the estimation of the instability stress ratios. Thus, the resistance to static liquefaction (represented as the distance between the origin and the instability surface) changes as a function of the Lode angle and fabric anisotropy. In agreement with experimental results, the instability stress ratios estimated from the derived instability criteria are dependent on b and  $\alpha_{\sigma}$  and can also be significantly influenced by the initial fabric, which highlights coupling effects between the loading and fabric evolution. For example, the onset of instability for a given Lode angle and an increasing  $\alpha_{\sigma}$  can be promoted or not, depending on the interactions between the loading and fabric directions.

#### 7 ACKNOWLEDGEMENTS

This material is based upon work supported by the National Science Foundation under Grant No 2013947. Any opinions, findings, and conclusions or recommendations expressed in this material are those of the authors and do not necessarily reflect the views of the National Science Foundation.

#### 8 REFERENCES

- Andrade, J. E., Ramos, A. M., & Lizcano, A. (2013). Criterion for flow liquefaction instability. *Acta Geotechnica*, 8(5), 525–535.
- Been, K., & Jefferies, M. G. (1985). A state parameter for sands. Géotechnique, 35(2), 99–112.
- Bokkisa, S. V., Macedo, J., Petalas, A. L., & Arson, C. (2022). Assessing static liquefaction triggering considering fabric anisotropy effects under the ACST framework. *Computers and Geotechnics*, *148*, 104796. https://doi.org/https://doi.org/10.1016/j.compgeo.2022.104796
- Dafalias, Y. F., & Manzari, M. T. (2004). Simple Plasticity Sand Model Accounting for Fabric Change Effects. *Journal of Engineering Mechanics*, 130(6), 622–634. https://doi.org/10.1061/(asce)0733-9399(2004)130:6(622)
- Gao, Z., & Zhao, J. (2015). Constitutive modeling of anisotropic sand behavior in monotonic and cyclic loading. *Journal of Engineering Mechanics*, 141(8), 4015017.
- Georgiannou, V. N., & Tsomokos, A. (2008). Comparison of two fine sands under torsional loading. *Canadian Geotechnical Journal*, 45(12), 1659–1672.
- Ishihara, K. (1993). Liquefaction and flow failure during earthquakes. *Geotechnique*, 43(3), 351–451. Thomas Telford Ltd.
- Lade, P. v. (1999). Instability of granular materials. In *Physics and mechanics of soil liquefaction* (pp. 3–16). Rotterdam: Balkema.
- Li, X. S., & Dafalias, Y. F. (2012). Anisotropic Critical State Theory: Role of Fabric. *Journal of Engineering Mechanics*, 138(3), 263–275. https://doi.org/10.1061/(asce)em.1943-7889.0000324
- Miura, S., & Toki, S. (1982). A sample preparation method and its effect on static and cyclic deformation-strength properties of sand. *Soils and Foundations*, 22(1), 61–77.
- Najma, A., & Latifi, M. (2017). Analytical definition of collapse surface in multiaxial space as a criterion for flow liquefaction occurrence. *Computers and Geotechnics*, 90, 120–132. https://doi.org/10.1016/j.compgeo.2017.06.005
- Najma, A., & Latifi, M. (2018). Collapse surface approach as a criterion of flow liquefaction occurrence in 3D FEM models. *Soil Dynamics and Earthquake Engineering*, 107, 164–178.
- Petalas, A. L., Dafalias, Y. F., & Papadimitriou, A. G. (2020). SANISAND-F: Sand constitutive model with evolving fabric anisotropy. *International Journal of Solids and Structures*, 188–189, 12–31. https://doi.org/10.1016/j.ijsolstr.2019.09.005

- Sadrekarimi, A. (2014). Effect of the mode of shear on static liquefaction analysis. *Journal of Geotechnical and Geoenvironmental Engineering*, 140(12), 4014069.
- Sze, H. Y., & Yang, J. (2014). Failure Modes of Sand in Undrained Cyclic Loading: Impact of Sample Preparation. *Journal of Geotechnical and Geoenvironmental Engineering*, 140(1), 152–169. https://doi.org/10.1061/(asce)gt.1943-5606.0000971
- Yang, Z. X., Lit, X. S., & Yang, J. (2008). Quantifying and modelling fabric anisotropy of granular soils. *Geotechnique*, 58(4), 237–248. https://doi.org/10.1680/geot.2008.58.4.237
- Yoshimine, M., Ishihara, K., & Vargas, W. (1998). Effects of principal stress direction and intermediate principal stress on undrained shear behavior of sand. *Soils and Foundations*, 38(3), 179–188.
- Zhu, H.-H., Wang, Z.-Y., Shi, B., & Wong, J. K.-W. (2016). Feasibility study of strain based stability evaluation of locally loaded slopes: Insights from physical and numerical modeling. *Engineering Geology*, 208, 39–50.